



Adsorption of CO₂ on Heterostructures of Bi₂O₃ Nanocluster-Modified TiO₂ and the Role of Reduction in Promoting CO₂ Activation

Nolan, M. (2018). Adsorption of CO₂ on Heterostructures of Bi₂O₃ Nanocluster-Modified TiO₂ and the Role of Reduction in Promoting CO₂ Activation. *ACS Omega*, 3(10), 13117-13128.
<https://doi.org/10.1021/acsomega.8b01957>

[Link to publication record in Ulster University Research Portal](#)

Published in:
ACS Omega

Publication Status:
Published (in print/issue): 12/10/2018

DOI:
[10.1021/acsomega.8b01957](https://doi.org/10.1021/acsomega.8b01957)

Document Version
Publisher's PDF, also known as Version of record

General rights

Copyright for the publications made accessible via Ulster University's Research Portal is retained by the author(s) and / or other copyright owners and it is a condition of accessing these publications that users recognise and abide by the legal requirements associated with these rights.

Take down policy

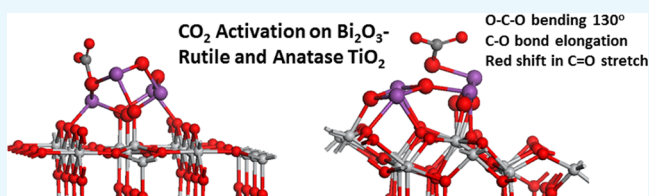
The Research Portal is Ulster University's institutional repository that provides access to Ulster's research outputs. Every effort has been made to ensure that content in the Research Portal does not infringe any person's rights, or applicable UK laws. If you discover content in the Research Portal that you believe breaches copyright or violates any law, please contact pure-support@ulster.ac.uk.

Adsorption of CO₂ on Heterostructures of Bi₂O₃ Nanocluster-Modified TiO₂ and the Role of Reduction in Promoting CO₂ Activation

Michael Nolan*

Tyndall National Institute, UCC, Lee Maltings, Dyke Parade, Cork T12 R5CP, Ireland

ABSTRACT: The capture and conversion of CO₂ are of significant importance in enabling the production of sustainable fuels, contributing to alleviating greenhouse gas emissions. While there are a number of key steps required to convert CO₂, the initial step of adsorption and activation by the catalyst is critical. Well-known metal oxides such as oxidized TiO₂ or CeO₂ are unable to promote this step. In addressing this difficult problem, a recent experimental work shows the potential for bismuth-containing materials to adsorb and convert CO₂, the origin of which is attributed to the role of the bismuth lone pair. In this paper, we present density functional theory (DFT) simulations of enhanced CO₂ adsorption on heterostructures composed of extended TiO₂ rutile (110) and anatase (101) surfaces modified with Bi₂O₃ nanoclusters, highlighting in particular the role of heterostructure reduction in activating CO₂. These heterostructures show low coordinated Bi sites in the nanoclusters and a valence band edge that is dominated by Bi–O states, typical of the Bi³⁺ lone pair. The reduction of Bi₂O₃–TiO₂ heterostructures can be facile and produces reduced Bi²⁺ and Ti³⁺ species. The interaction of CO₂ with this electron-rich, reduced system can produce CO directly, reoxidizing the heterostructure, or form an activated carboxyl species (CO₂[−]) through electron transfer from the reduced heterostructure to CO₂. The oxidized Bi₂O₃–TiO₂ heterostructures can adsorb CO₂ in carbonate-like adsorption modes, with moderately strong adsorption energies. The hydrogenation of the nanocluster and migration to adsorbed CO₂ is feasible with H-migration barriers less than 0.7 eV, but this forms a stable COOH intermediate rather than breaking C–O bonds or producing formate. These results highlight that a reducible metal oxide heterostructure composed of a semiconducting metal oxide modified with suitable metal oxide nanoclusters can activate CO₂, potentially overcoming the difficulties associated with the difficult first step in CO₂ conversion.



1. INTRODUCTION

Increasing energy demand is leading to fossil fuel supply issues, and the use of fossil fuels has pushed the atmospheric CO₂ concentration to 410 ppm. Continuing CO₂ emissions are projected to result in a higher than 2 °C rise in average global temperatures. Given these severe societal problems, there is an urgent need to find materials that can convert the CO₂ produced by the combustion of fossil fuels back to the fuels or to the precursors for the production of more useful chemicals. This will reduce our reliance on unsustainable fossil fuels and contribute to curbing anthropogenic CO₂ emissions. The solar-driven photoreduction or thermal reduction of CO₂ to CO or directly to liquid fuels will enable a sustainable approach to producing fuels and storing solar energy in high-energy chemical bonds.^{1–11}

Using solar energy, for example, through solar concentrators, coupled with catalysts that can promote activation of CO₂ to drive the CO₂ reduction process, is an attractive strategy to meet this ambitious aim. However, to date, there are no practical catalysts that can exploit solar energy to efficiently reduce CO₂ to useful chemical species. A range of different catalysts for CO₂ conversion using electrocatalysis, thermochemical catalysis, and photocatalysis has been investigated in recent years, and an example of such a photocatalyst is Pt-

modified TiO₂ nanotubes.^{8,12,13} However, the efficiencies for methane production are extremely low, and Pt will never be an economically viable catalyst for large-scale CO₂ conversion.

Irrespective of how electrons are provided to reduce CO₂, the key step in any CO₂ capture and use/conversion process is the initial adsorption of CO₂, which should promote the “activation” of the molecule. This activation can be a charge transfer to CO₂, distortions to the molecular structure such as bending of O–C–O away from the linear elongations in the molecular C–O distances, or hydrogenation. CO₂ should either dissociate to a CO molecule or undergo hydrogenation to produce methane or methanol, via formate or carboxyl pathways. The activation should also avoid the production of overstabilized inactive surface-bound carbonates which would poison the catalyst.

In recent years, catalysts based on metallic Cu, oxide-derived Cu, or Cu with mixed oxidation states have gained great interest and have been demonstrated to reduce CO₂ to useful molecules such as methane, methanol, or ethanol.^{14–22} Recent experimental work indicates the ability of nanocatalysts

Received: August 9, 2018

Accepted: August 16, 2018

Published: October 12, 2018

containing a mix of Cu^+ and Cu^{2+} oxidation states and in oxide-like structures to promote CO_2 reduction^{1,2,10,14–16,18,19,21–29} and this includes Cu metal, oxide-derived Cu, and mixed oxidation state Cu. Modeling the interaction of CO_2 with copper oxides using density functional theory (DFT) has provided useful results for further development of catalysts for CO_2 conversion. Wu et al. studied the adsorption of CO_2 at the $\text{Cu}_2\text{O}(111)$ surface in which excess electrons were produced through the formation of oxygen vacancies¹⁸ and found that dissociative adsorption of CO_2 was thermodynamically unfeasible, and although a $\text{CO}_2^{\delta-}$ anion could be formed, this was not favorable, and hence excess electrons are not necessarily sufficient to promote CO_2 capture and conversion. Wu et al. also studied the adsorption of CO_2 and its derivatives at $\text{Cu}_2\text{O}(111)$ using hybrid DFT²¹ and found that only the adsorption of linear CO_2 was favorable. This is supported by the work of Benavid and Carter who showed that physisorption of linear CO_2 is favored over adsorption of bent anionic CO_2^- .¹⁹ Mishra and colleagues reported strong CO_2 chemisorption at the high-energy Cu–O-terminated (110) surface of Cu_2O ¹⁵ and exothermic adsorption of CO_2 at the high-energy (011) surface of CuO .² Uzunova et al. studied the conversion of CO_2 to methanol on Cu_2O nanolayers and clusters¹⁶ using hybrid DFT. The authors considered water as the source of H atoms for the hydrogenation of CO_2 and described a reaction pathway from a carboxyl group ($^*\text{COOH}$) to formic acid, which was the rate-limiting step, and then onto formaldehyde and finally methanol. This work would suggest other pathways for CO_2 conversion beyond the dissociation into CO. In the work of Favaro et al.,²⁴ a model of Cu with subsurface oxygen was required for copper to adsorb CO_2 in the first place and understand the experimental findings. However, despite these advances, there still remains an urgent need from both a fundamental and a technoeconomic perspective to discover new materials that can activate and reduce CO_2 , in particular to produce sustainable fuels, particularly if renewable energy can be used, either for electroreduction or to produce renewable hydrogen from water.

Another popular metal oxide is titanium dioxide, and the adsorption of CO_2 at different titania surfaces and nanostructures has been widely studied. The roles of excess electrons introduced by oxygen vacancies, low coordinated atomic sites, and the surface structure in CO_2 adsorption and activation have been discussed.^{30–32} The presence of excess electrons and holes was shown to influence the adsorption and activation of CO_2 at rutile (110), and both bent CO_2^- anion and CO_2^+ cation configurations were identified from the DFT calculations.³³ Lee and Kanai³² used DFT to explore the difference between anatase (101) and a nanostructured TiO_2 quantum dot for CO_2 activation and hydrogenation. They found that the TiO_2 quantum dot promoted CO_2 activation and hydrogenation when compared to the extended anatase (101) surface. Yang and colleagues showed that subnanometer Pt clusters supported on the anatase (101) surface enhanced CO_2 activation through the provision of additional adsorption sites and the transfer of electron density to the TiO_2 substrate.³⁴

Various other metal oxides have been investigated for CO_2 conversion, and several theoretical studies have been conducted into the reaction pathways involving the hydrogenation of CO and CO_2 at a variety of catalytic surfaces, including Cu/ CeO_2 and Cu/ $\text{CeO}_2/\text{TiO}_2$ ¹⁷ or Cu/ $\text{ZnO}/\text{Al}_2\text{O}_3$.³⁵ An enhanced photoreduction of CO_2 with H_2O

vapor has been reported for dispersed $\text{CeO}_2/\text{TiO}_2$.³⁶ Here, the ceria is modeled as a small cluster supported on rutile TiO_2 , similar to the work on water gas shift,^{37–39} and the role of Ce^{3+} in visible light absorption, photogenerated charge separation, and strengthening of the CO_2 –surface bonding was highlighted.

Recent experimental works from Rosenthal and co-workers^{40–43} and Walker et al.⁴⁴ strongly suggest that non-transition-metal based catalysts, in particular those containing bismuth or tin, are able to activate CO_2 or convert it to other molecules with good efficiency. The catalysts in refs^{40,43} are composed of Bi–glassy carbon and use ionic liquids or Bi nanoparticles, which have large amounts of Bi^{3+} . The former materials can convert CO_2 to alcohols with high efficiency, and even though ionic liquids are used, the role of Bi in the catalyst remains crucial to promote the conversion of CO_2 .

The bismuth pyrochlore oxide $\text{Bi}_2\text{Ti}_2\text{O}_7$ was studied in ref 44 and was shown to have high CO_2 chemisorption capacity. In this system, low-energy ion scattering (LEIS) shows clearly that the surface layer is terminated by a bismuth oxide layer. This surface structure arises from the well-known stereochemical lone pair in Bi^{3+} .^{45,46} By contrast, in the pyrochlore $\text{Y}_2\text{Ti}_2\text{O}_7$, there is no surface enrichment with Y^{3+} (lacking the lone pair). This Bi-oxide-terminated pyrochlore was examined for its capacity to adsorb and activate CO_2 using infrared spectroscopy. The features in the infrared spectrum corresponding to the adsorbed CO_2 were clearly present upon heating to 308 K. $\text{Y}_2\text{Ti}_2\text{O}_7$, by contrast, does not strongly adsorb CO_2 . This suggests that the adsorption of CO_2 arises from the presence of Bi^{3+} and a bismuth oxide surface layer in the pyrochlore surface.

From the studies in refs,^{40,44} it is reasonable to propose that the presence of the Bi^{3+} cation, with its stereochemically active lone pair, in a Bi-oxide structure will be active in promoting the interaction of Bi-containing oxides with CO_2 . However, the mechanism of CO_2 adsorption and conversion on Bi^{3+} -containing materials, as a good exemplar of the p-block metal oxides, needs to be further investigated, and this is one of the aims of this study.

Previously, we have used first-principles DFT simulations to design heterostructured materials which are composed of TiO_2 (rutile or anatase) surfaces modified with metal oxide nanoclusters. In our earlier work, the emphasis has been on new heterostructured materials with predicted visible light absorption^{47–59} and reduced charge recombination.^{48–52,60–62} We have recently studied the interaction of molecules, such as CO_2 , with tin(II) oxide,⁴⁷ zirconia,⁴⁷ manganese oxide,⁶³ alkaline earth oxide,⁶⁴ and ceria⁶⁵ nanocluster-modified TiO_2 heterostructures. We have found that such nanocluster-modified TiO_2 heterostructures can adsorb CO_2 ,⁴⁷ but that some heterostructures, such as reduced MnO_x – TiO_2 , do not show favorable CO_2 adsorption, even though reduced cations are present.⁶³ There is still much work to be done to understand the factors that drive CO_2 activation on metal oxides.

In the present paper, we take the ideas from the experimental work on CO_2 activation on Bi-containing materials, the ability of nanostructures to activate CO_2 , and the activity of nanocluster-modified TiO_2 and use first-principles DFT to examine in detail the interaction and adsorption of CO_2 at Bi_2O_3 nanocluster-modified rutile and anatase TiO_2 . We explore the role of the Bi-oxide' the low coordinated sites in nanoclusters and reduction of the Bi_2O_3 –

TiO₂ heterostructures in CO₂ adsorption and activation. In some examples, we examine further interaction with hydrogen for the first steps in hydrogenation and formation of intermediates such as COOH or HCOO. The role of heterostructure reduction in CO₂ activation is crucial, wherein the charge transfer from the reduced oxide heterostructure can result in the formation of a carboxylate or direct formation of CO.

2. METHODS

In the DFT computations, we follow our approach from previous work⁶¹ and prepare heterostructures of Bi₂O₃ nanoclusters supported on the extended low-energy rutile (110) and anatase (101) surfaces; although other rutile and anatase surfaces can be present in, for example, typical TiO₂ nanoparticles, these are the dominant surface facets and are well-studied.

All DFT computations use a three-dimensional periodic surface slab within the VASP code^{66–69} and a plane-wave basis set to describe the valence electrons. Projector-augmented wave potentials,^{70,71} with 4, 5, 6, 4, and 1 valence electrons for Ti, Bi, O, C, and H, respectively, describe the core–valence electron interactions, and this setup was extensively tested in our earlier work on Bi₂O₃-modified TiO₂.⁶¹ The cutoff for the kinetic energy is 396 eV, and the exchange–correlation functional is the Perdew–Wang 91⁷² approximation. A Monkhorst–Pack (2 × 1 × 1) *k*-point sampling grid is used. For consistency with our previous work, we apply the DFT + *U* approach^{73,74} to describe the Ti 3d states, with a value of *U* = 4.5 eV. The convergence criteria for the electronic and ionic relaxations are 0.0001 eV and 0.02 eV/Å. Methfessel–Paxton smearing is used with $\sigma = 0.1$ eV (also for the broadening of the peaks in the projected density of states). We use the Newton–Raphson relaxation algorithm, and all calculations are spin-polarized throughout, with no constraints on the spin.

The rutile (110) surface is terminated by twofold coordinated bridging O atoms, with threefold coordinated in-plane oxygen atoms in the surface layer. In the same layer, the Ti atoms take fivefold and sixfold coordinations. The anatase (101) surface is characterized by twofold coordinated oxygen atoms terminating the surface layer, and the outermost Ti atoms are fivefold coordinated. Surface supercell expansions of (2 × 4) and (4 × 2) are employed for rutile and anatase, respectively, and the vacuum gap in all cases is 12 Å.

In forming these composite structures, we first relax the gas-phase metal oxide nanoclusters and the unmodified rutile and anatase surfaces using the same computational setup described above. The oxide nanocluster modifier is adsorbed at the TiO₂ surfaces in different configurations, and each of these are relaxed, as described in refs.^{48,57,61,75} We selected the most stable Bi₂O₃–TiO₂ composites for the study of CO₂ activation in the present paper. We will use the term Bi₂O₃–TiO₂ throughout this paper to indicate the general Bi₂O₃ nanocluster-modified TiO₂ heterostructure, using the precise nanocluster composition and TiO₂ surface when necessary.

The stability of the heterostructure is characterized by the computed nanocluster adsorption energy, E^{ads}

$$E^{\text{ads}} = E[(\text{Bi}_2\text{O}_3)_n - \text{TiO}_2] - \{E[(\text{Bi}_2\text{O}_3)_n] + E[\text{TiO}_2]\} \quad (1)$$

where $E[(\text{Bi}_2\text{O}_3)_n - \text{TiO}_2]$ is the computed total energy of the Bi₂O₃ nanocluster-modified TiO₂ surface (in which *n* is the number of Bi₂O₃ units in the nanocluster, so that in this paper

n = 2 or 3), $E[(\text{Bi}_2\text{O}_3)_n]$ is the computed total energy of the free (Bi₂O₃)_{*n*} nanocluster, and $E[\text{TiO}_2]$ is the computed total energy of the unmodified TiO₂ (rutile/anatase) surface.

The reduction of the Bi₂O₃–TiO₂ heterostructures is studied by removing oxygen from the nanocluster modifier (which is always more stable than removing oxygen from the TiO₂ support) and computing the formation energy of the oxygen vacancy as follows

$$E^{\text{vac}} = E\{((\text{Bi}_2\text{O}_{3-x})_n - \text{TiO}_{2-x}) + 1/2E(\text{O}_2)\} - E((\text{Bi}_2\text{O}_3)_n - \text{TiO}_2) \quad (2)$$

where $E\{((\text{Bi}_2\text{O}_{3-x})_n - \text{TiO}_2)\}$ is the total energy of the Bi₂O₃–TiO₂ composite with one oxygen removed and $1/2E(\text{O}_2)$ is the reference energy for oxygen, namely half the total energy of the O₂ molecule. We correct the oxygen vacancy formation energy for entropy, which, at 298 K, is 0.60 eV. Despite the known errors in the DFT energy of the reference O₂ molecule, the trends in oxygen vacancy formation are independent of this error. We also use ab initio thermodynamics to determine the stability of the reduced Bi₂O₃–TiO₂ heterostructures formed by removing oxygen over a range of temperatures.

To analyze the stability of the reduced heterostructured models when exposed to an environment of oxygen, we use the DFT-derived total energies as an input into an atomistic thermodynamics framework, which considers the effect of the surrounding gas phase as a reservoir that is in thermodynamic equilibrium with the heterostructure. If we assume that the oxygen reservoir exchanges particles with the system without affecting its chemical potential, the oxygen vacancy formation energy is calculated as follows

$$E^{\text{vac}} = [E(\text{Bi}_2\text{O}_{3-\delta} - \text{TiO}_2) + N_{\text{O}}\mu_{\text{O}}(p, T)] - E(\text{Bi}_2\text{O}_3 - \text{TiO}_2) \quad (3)$$

where $E(\text{Bi}_2\text{O}_{3-\delta} - \text{TiO}_2)$ and $E(\text{Bi}_2\text{O}_3 - \text{TiO}_2)$ are the total DFT energies of the Bi₂O₃–TiO₂ heterostructures with and without the oxygen vacancy, *N*_O is the number of oxygen atoms removed, and $\mu_{\text{O}}(p, T)$ is the chemical potential of oxygen. Approximating oxygen as an ideal gas, we explicitly introduce pressure and temperature in our model through the analytic relation between the chemical potentials and the temperature and pressure of the two gas reservoirs as follows

$$\mu_{\text{O}}(p, T) = \left[\frac{1}{2}E_{\text{O}_2} + \mu'_{\text{O}_2} + k_{\text{B}}T \ln\left(\frac{p_{\text{O}_2}}{p^0}\right) \right] \quad (4)$$

Here, *T* and *p* represent the temperature and partial pressure of oxygen, *p*⁰ denotes atmospheric pressure, and *k*_B is the Boltzmann constant. μ' is the energetic term that includes contributions from the rotations and vibrations of the molecule, as well as the ideal-gas entropy at 1 atm, which can be calculated or taken from the experimental values listed in the thermodynamic tables. Thus, for a given pressure, the stability of oxygen vacancies can be determined over a range of temperatures.

The CO₂ adsorption energy at Bi₂O₃-modified TiO₂ heterostructures is defined in eq 5

$$E^{\text{ads}} = E(\text{CO}_2 @ (\text{Bi}_2\text{O}_3)_n - \text{TiO}_2) - \{E((\text{Bi}_2\text{O}_3)_n - \text{TiO}_2) + E(\text{CO}_2)\} \quad (5)$$

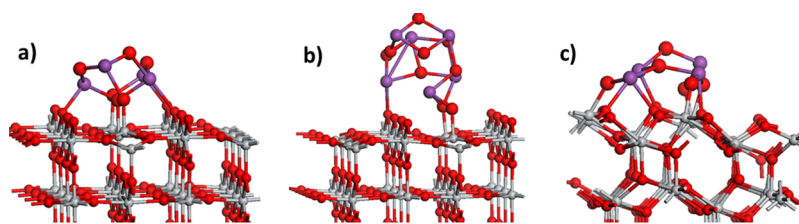


Figure 1. Relaxed atomic structure for Bi_2O_3 nanocluster-modified rutile (110) and anatase (101). (a) Bi_4O_6 -rutile (110), (b) Bi_6O_9 -rutile (110), and (c) Bi_4O_6 -anatase (101). The color coding in this and subsequent figures is Ti = light gray sphere, O = red sphere, and Bi = purple sphere. Bi and O atoms in the adsorbed nanoclusters are depicted by larger radius spheres.

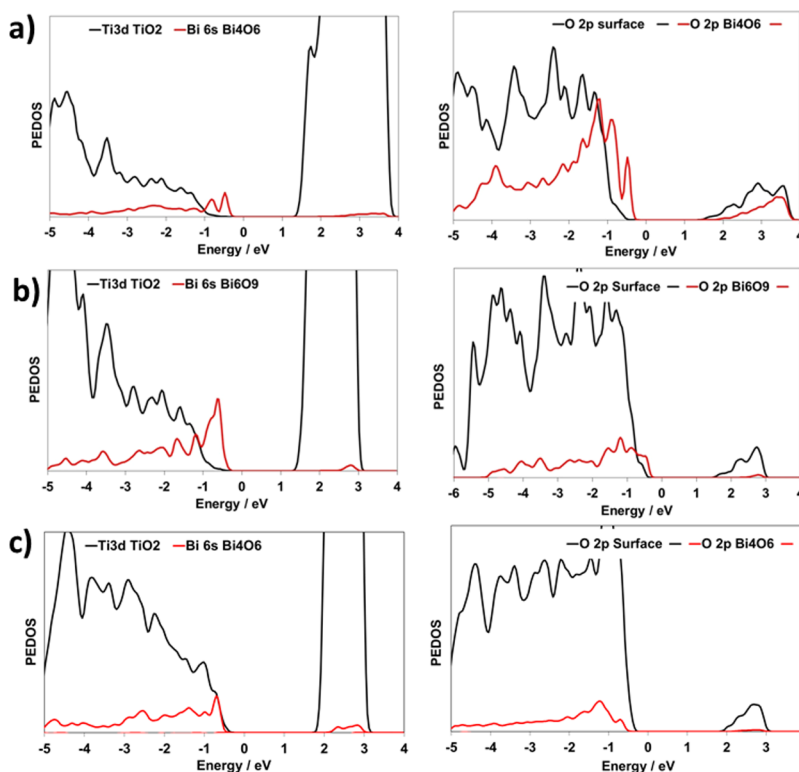


Figure 2. PEDOS projected onto the Bi 6s, Ti 3d, and O 2p states (nanocluster and surface) for (a) Bi_4O_6 rutile (110), (b) Bi_6O_9 -rutile (110), and (c) Bi_4O_6 -anatase (101). The zero of energy in all cases is the Fermi level. The left panels show the cation PEDOS and the right panels show the oxygen 2p PEDOS.

where $E(\text{CO}_2@(\text{Bi}_2\text{O}_3)_n-\text{TiO}_2)$ is the computed total energy of the relaxed adsorption structure of CO_2 at Bi_2O_3 -modified TiO_2 composites, whether stoichiometric or reduced. We examined many CO_2 adsorption structures, and those shown in the following text are the most stable that we have found. Although van der Waals corrections can be added to these computations, we have tested and found that the change in the adsorption energies is ca. 0.15 eV, which is not significant compared to the magnitude of the computed CO_2 adsorption energies, and furthermore, there is no effect of the inclusion of vdW corrections on the relative stability of different CO_2 adsorption structures.

3. RESULTS AND DISCUSSION

3.1. Bi_2O_3 -Modified Rutile and Anatase TiO_2 Heterostructures. Figure 1 shows the atomic structures of the nanocluster-modified anatase (101) and rutile (110) surfaces of Bi_4O_6 and Bi_6O_9 . We have described these heterostructured systems in detail in previous work,⁶¹ and we briefly summarize the key features required for this paper. The adsorption

energies can be computed relative to the corresponding gas-phase stoichiometric Bi_2O_3 nanoclusters, and these are −5.18, −5.18, and −5.72 eV for Bi_4O_6 -rutile, Bi_6O_9 -rutile, and Bi_4O_6 -anatase, respectively. If we consider these energies in terms of the deposition of the nanoclusters at very low loading/coverage through atomic layer deposition, chemisorption–calcination, or incipient wetness impregnation, then the above energies can be related to the desorption of the Bi_2O_3 nanoclusters from the TiO_2 supports. The magnitude of the computed energies indicates a strong binding of the nanocluster modifiers at both TiO_2 surfaces and suggests they would only desorb at very high temperatures.

We can also consider the stability against sintering into larger nanoclusters. In the gas phase, the gain in energy when two nanoclusters of composition Bi_2O_3 coalesce into a larger Bi_4O_6 nanocluster is −6.1 eV, and the coalescence of a gas-phase Bi_2O_3 and a gas-phase Bi_4O_6 nanocluster results in a gain of 3.1 eV. On the surface, we use the total energies of the bismuth oxide nanocluster-modified rutile heterostructures to assess the nanocluster stability against coalescence into larger

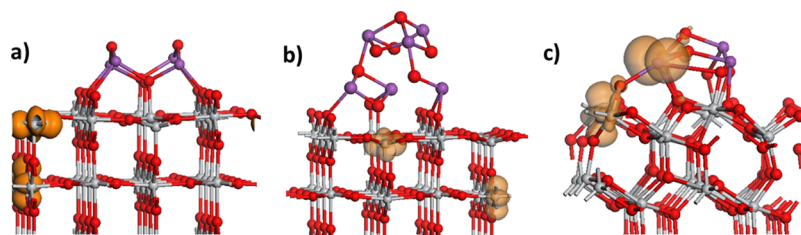


Figure 3. Atomic structure and spin density isosurfaces of the most stable reduced Bi_2O_3 – TiO_2 heterostructures: (a) Bi_4O_6 –rutile (110), (b) Bi_6O_9 –rutile (110), and (c) Bi_4O_6 –anatase (101). Spin density isosurfaces enclose spin densities up to 0.02 electrons/ \AA^3 . The color coding of the atoms is the same as in Figure 1.

nanoclusters.⁷⁵ For the example of Bi_2O_3 and Bi_4O_6 coalescing to a Bi_6O_9 nanocluster

$$\Delta E = (E^{\text{Bi}_6\text{O}_9\text{-rutile}} + E^{\text{rutile}(110)}) - (E^{\text{Bi}_2\text{O}_3\text{-rutile}} + E^{\text{Bi}_4\text{O}_6\text{-rutile}})$$

The computed energy is +2.69 eV against coalescence of the two smaller nanoclusters supported on rutile (110). Thus, when the Bi_2O_3 nanoclusters are supported on rutile or anatase, they will be stable against desorption or aggregation. The high stability of the supported Bi_2O_3 nanoclusters is primarily driven by the formation of new interfacial bonds between the nanocluster and the surface. We also note that the extensive work of Graciani et al. on ceria– TiO_2 used small Ce_2O_3 species supported on rutile (110),^{38,39} which were also shown to be highly stable.

On Bi_4O_6 –rutile, two Bi cations bind to the bridging surface oxygen, with typical Bi–O distances of 2.17 Å. These Bi cations are threefold coordinated, whereas the remaining Bi cations are twofold coordinated. Three oxygen atoms from the nanocluster bind to the fivefold coordinated Ti surface atoms, with the Ti–O distances in the range of 1.83–2.05 Å. In the Bi_6O_9 –rutile nanocluster, one Bi cation binds to a bridging oxygen, with a Bi–O distance of 2.37 Å. Two oxygen atoms from the nanocluster bind to the surface Ti atoms, with the Ti–O distances of 1.94 and 1.86 Å. Here, the terminal Bi cations, furthest away from the cluster–surface interface, are threefold coordinated, and there are twofold coordinated oxygen sites in the nanocluster.

In Bi_4O_6 –anatase, three Bi cations bind to the surface oxygen, with the Bi–O distances of 2.14, 2.14, 2.24, and 2.17 Å. The two Bi cations furthest away from the cluster–surface interface are threefold coordinated and the remaining Bi cations are fourfold coordinated. Four oxygen atoms in the nanocluster bind to the surface Ti, with the distances Ti–O in the range of 1.87–2.06 Å. There are three twofold coordinated oxygen sites: one is the terminal oxygen in the nanocluster and the remaining two sites bridge the nanocluster and the anatase (101) surface.

The other important aspect of the Bi_2O_3 – TiO_2 composites for the interaction with CO_2 is their electronic properties, and in Figure 2 we show the projected electronic density of states (PEDOS) for the Bi_2O_3 –rutile and Bi_2O_3 –anatase systems. Bi^{3+} is an interesting species as it has a stereochemically active lone pair, which results in the presence of Bi-derived electronic states at the top of the valence band. This gives rise to the distorted structure of bulk Bi_2O_3 ⁴⁶ and the Bi-rich surface region in the pyrochlore $\text{Bi}_2\text{Ti}_2\text{O}_7$.⁴⁴ The other metal oxides with +3 cations do not show these structural distortions.

In the PEDOS of the Bi_2O_3 – TiO_2 heterostructures, the Bi electronic states are present at the valence band edge of all the

composite systems studied. For modified rutile (110), we see Bi (6s + 6p) and O 2p states originating from the nanoclusters lying at a higher energy than the corresponding TiO_2 valence and conduction band edges, which should result in a small red shift in light absorption. For anatase, the Bi_2O_3 –derived states lie just below the anatase valence band edge, which results in no predicted red shift. The key finding is that the Bi states lie at the top of the valence band edge, and this can be important in the reduction or CO_2 adsorption on the Bi_2O_3 – TiO_2 heterostructures.

Finally, we present the results for the reduction of the Bi_2O_3 – TiO_2 heterostructures. The reduced heterostructures are prepared by removing oxygen atoms from the Bi_2O_3 nanoclusters and computing the oxygen vacancy formation energy. From a practical perspective, reduction can be facilitated by a thermochemical process using concentrated solar radiation or by the introduction of hydrogen in a redox process. Relaxing the structure after the removal of oxygen, the most stable reduced heterostructures are shown in Figure 3. The computed formation energies for the most stable oxygen vacancy sites are 1.75 eV (1.12 eV) for Bi_4O_6 –rutile (110), 1.64 eV (1.01 eV) for Bi_6O_9 –rutile (110), and 3.0 eV (2.37 eV) for Bi_4O_6 –anatase (101), where the formation energies corrected for $T\Delta S$ at 298 K are given in parentheses. These formation energies that show a moderate cost for oxygen vacancy formation in the supported Bi_2O_3 nanoclusters are notably smaller than that on the corresponding bare TiO_2 surfaces (3.5 eV for rutile (110) and 3.6–4.1 eV for anatase (101)⁷⁶), so that reduction should be possible under moderate conditions. The other oxygen sites have formation energies larger than 2 eV on Bi_4O_6 –rutile and between 3.4 and 3.7 eV on Bi_4O_6 –anatase. Figure 4 shows the stability of the most stable oxygen vacancy sites in each heterostructure as a function of temperature at a pressure of 1 atm. From this plot, we can

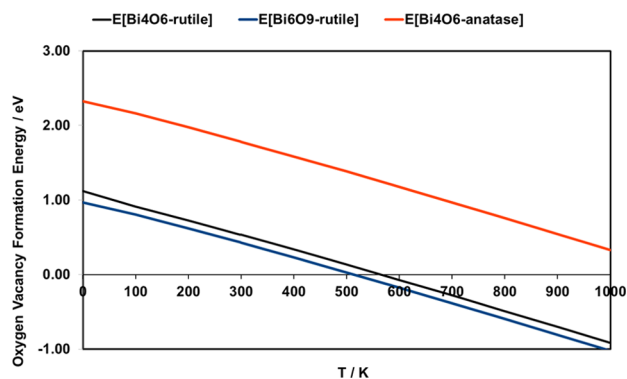


Figure 4. Computed oxygen vacancy formation energy for Bi_2O_3 –modified TiO_2 as a function of temperature at a pressure of 1 atm.

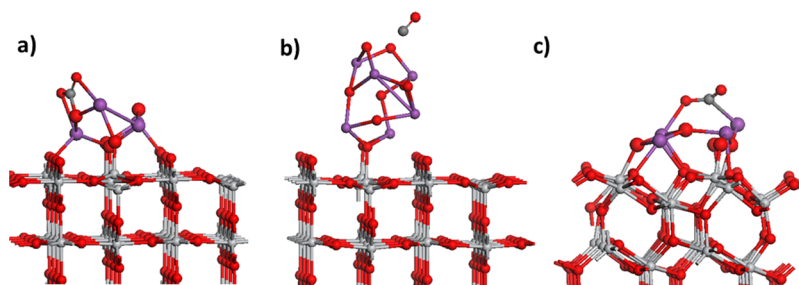


Figure 5. Atomic structure of the most stable CO₂ adsorption structures on reduced Bi₂O₃–TiO₂ composites: (a) Bi₄O₆–rutile (110), (b) Bi₆O₉–rutile (110), and (c) Bi₄O₆–anatase (101). The color coding is the same as in Figure 1, with an additional inclusion of a gray sphere for carbon. The Bi and O atoms in the supported Bi₂O₃ nanoclusters are depicted with larger diameter spheres.

see that reduction should take place at 500–600 K, which is certainly feasible in the context of CO₂ reduction/conversion processes. For the rutile-supported Bi₆O₉ nanocluster, the larger formation energy of the vacancy clearly results in a higher temperature for vacancy formation, although this is still notably lower than that on bare rutile (110).

After the reduction of the Bi₂O₃ nanoclusters, the local atomic structure shows some changes. On Bi₄O₆–rutile (110), the removal of oxygen results in the formation of a structure that shows symmetry, with two twofold coordinated oxygen atoms terminating the nanocluster. The Bi cations are threefold coordinated, and each Bi atom binds to a bridging oxygen atom from the rutile (110) surface, with the Bi–O distances in the range of 2.17–2.18 Å. Furthermore, each Bi atom also coordinates to one oxygen from the nanocluster, which itself binds to a surface Ti atom, with the Bi–O distances of 2.07–2.15 Å and Ti–O distances of 2.03 Å.

On Bi₆O₉–rutile, the formation of the most stable oxygen vacancy results in small changes to the nanocluster structure. Two Bi cations are coordinated to the surface-bridging oxygen sites, with the Bi–O distances of 2.20–2.23 Å. Two nanocluster oxygen bind to the surface fivefold coordinated Ti, with the Ti–O distances of 1.89 and 2.02 Å, whereas after relaxation, four oxygen atoms take a twofold coordination environment by breaking the bonds with Bi cations (giving long Bi–O distances of 2.51 and 2.56 Å).

On Bi₄O₆–anatase, two Bi cations are threefold coordinated and the remaining cations are fourfold coordinated. The typical Bi–O distances range from 1.86 to 2.15 Å, and the Bi–O distances to the surface range from 2.12 to 2.16 Å. One oxygen atom from the surface migrates outward to bind to a Bi cation in the nanocluster, with three oxygen atoms in the nanocluster binding to the surface Ti sites; the Bi–O distances are in the range 1.86–1.90 Å.

The localization of the two electrons released upon removal of the neutral oxygen atom is shown by the spin density isosurfaces in Figure 3. For both Bi₂O₃ nanocluster-modified rutile (110) composites, the electrons preferentially localize on the Ti sites in the rutile (110) surface, with the computed Ti Bader charges of +1.65/1.71 electrons in Bi₄O₆–rutile and +1.65/1.69 electrons in Bi₆O₉–rutile and spin magnetization in the range 0.92–0.94 μ_B. For reference, Ti⁴⁺ cations have computed Bader charges of +1.30 electrons and zero spin magnetization. The first electron localizes on a subsurface Ti site and the second electron localizes onto a surface fivefold coordinated Ti site that has no interaction with the supported nanocluster. These values are typical of the reduced Ti³⁺ species in rutile (110).

In contrast, on Bi₄O₆–anatase (101), the two electrons localize on a surface fivefold coordinated Ti³⁺ site and on a Bi site in the nanocluster, which results in the formation of a reduced Bi²⁺ species. The computed Bader charges are +1.74 electrons on Ti and +2.99 electrons on Bi; the latter is comparable to a computed Bi Bader charge of +2.1 electrons for Bi³⁺ cations, indicating the reduction of the Bi species. The computed spin magnetizations on Ti and Bi are 0.96 and 0.7 μ_B. This Bi site binds to the oxygen that migrated out of the surface, and this particular oxygen bridges the two reduced Ti³⁺ and Bi²⁺ sites.

3.2. Adsorption of CO₂ at Reduced Bi₂O₃–TiO₂ Heterostructures. We now discuss the adsorption of CO₂ at the Bi₂O₃ nanocluster-modified TiO₂ heterostructures, and in this section we focus on the reduced heterostructures. We examined the interaction of the reduced Bi₂O₃–TiO₂ heterostructures with CO₂ in a number of adsorption configurations. Figure 5 shows the most stable relaxed structures after the relaxation of adsorbed CO₂ on each reduced Bi₂O₃–TiO₂ heterostructure. The computed interaction energies for CO₂ are –0.45 eV on reduced Bi₄O₆–rutile (110), –0.53 eV on reduced Bi₆O₉–rutile (110), and –0.93 eV on reduced Bi₄O₆–anatase (101). These energies indicate a moderately strong interaction between the initially reduced metal oxide heterostructure and the CO₂ molecule.

CO₂ binds to reduced Bi₄O₆–rutile (110) with the formation of two Bi–O bonds, with the Bi–O distances of 2.45 and 2.52 Å. The carbon of CO₂ binds to the oxygen in the nanocluster, with a C–O distance of 1.38 Å. The C–O distances in the adsorbed CO₂ are elongated to 1.27 Å, and the O–C–O angle is 130°. Thus, the CO₂ molecule adsorbs moderately exothermically on the reduced supported Bi₄O₆ nanocluster in a manner that can be considered carbonate-like with a tridentate adsorption configuration, although one of the C–O bonds is significantly longer than the typical C–O carbonate distance.

Examining the electronic structure in the CO₂–Bi₄O₆–rutile system, the computed Bader charges on the previously reduced Ti atoms are now +1.3 electrons, signifying the presence of oxidized Ti⁴⁺ species. Interestingly, we find that the charge on two Bi cations in the nanocluster changes to 2.8 and 3.2 electrons, indicating that these Bi cations are partially reduced. One of these Bi cations binds to the oxygen of CO₂, suggesting a rearrangement of charge upon CO₂ adsorption.

On Bi₆O₉–rutile (110), the relaxation of initially adsorbed CO₂ leads to spontaneous breaking of a C–O bond in the molecule, which results in the release of a free CO molecule, with no energy barrier to this process. Although one might expect a significant energy gain in breaking a C–O bond, we

have to consider that this process heals the vacancy site on the Bi_2O_3 nanocluster, which has a high stability, and there would also be an energy cost to break the C–O bond in the molecule. In any case, the key point is the exothermic release of CO.

When CO is released, the previous supported Bi_6O_9 nanocluster is reoxidized, with the Bi_6O_9 composition. Examining the atomic structure, we see that the free CO has a C–O distance of 1.14 Å, which is typical of the gas-phase CO, and the Bi–O distances are similar to those in the stoichiometric Bi_6O_9 -rutile system. In the Bi_6O_9 -rutile system, the computed Bader charges of Ti and Bi are +1.3 and +2.2 electrons, consistent with the presence of only oxidized Ti^{4+} and Bi^{3+} species. The electrons on the TiO_2 surface after reduction are therefore transferred to CO_2 to allow the formation of new Bi–O bonds and a free CO molecule.

To examine this in more detail and complete a redox cycle, we adsorb H_2 at the site of the oxygen species that results from CO_2 dissociation, that is, oxygen that reoxidized reduced Bi_6O_9 -rutile. Upon relaxation, a water molecule spontaneously forms, with an exothermic energy gain of 1.13 eV which reduces the Bi_6O_9 nanocluster; removal of water from the supercell requires 0.43 eV, and the reduced supported nanocluster is available for reaction with another CO_2 . Thus, the Bi_6O_9 nanocluster supported on rutile TiO_2 appears to show a pathway for CO_2 dissociation through a redox process involving water formation in a reverse water gas shift-like process.

Finally, on Bi_4O_6 -anatase (101), the computed Bader charges on the CO_2 molecule indicate a charge transfer of ca. 1.5 electrons to the molecule from the reduced composite. The computed Bader charges of 1.3 and 2.1 electrons on previously reduced Ti and Bi further support this electron transfer, which reoxidizes Ti and Bi. This process then results in the formation and stabilization of a carboxyl, CO_2^- species. This is one of the activated CO_2 species that is important in CO_2 conversion. In the gas phase, the potential required for the formation of CO_2^- is prohibitively high, but in the reduced Bi_2O_3 -modified anatase system, the presence of both low coordinated active sites and excess electrons after reduction appears to facilitate electron transfer to the adsorbed CO_2 molecule. In adsorbed carboxyl, the C–O distances are 1.25 and 1.27 Å, again showing a significant elongation over the free molecule. The bending of CO_2 upon interaction with the nanocluster is also apparent, with an O–C–O angle of 130° . CO_2 binds to the nanocluster through a Bi–O bond, which has a distance of 2.42 Å and a Bi–C bond of 2.37 Å involving a second Bi atom in the nanocluster.

The computed vibrational frequencies for CO_2 adsorbed on reduced heterostructures are shown in Table 1. The computed gas-phase vibrational modes of CO_2 are 2354, 1325, and 632 cm^{-1} , with the latter being degenerate. These correspond to the asymmetric C=O stretch, the symmetric C=O stretch, and the O–C–O bending mode. The large red shift in the C=O stretching mode of 760 and 767 cm^{-1} on Bi_4O_6 -rutile and Bi_4O_6 -anatase is consistent with the strong adsorption of CO_2 , as is the breaking of the degeneracy in the CO_2 bending mode upon adsorption. We note that on Bi_4O_6 -anatase the splitting of the degeneracy in the CO_2 bending mode is larger, the origin of which is likely due to one oxygen of CO_2 not binding with the Bi_2O_3 nanocluster. By contrast, the two oxygen atoms in CO_2 bind with the nanocluster in Bi_4O_6 -rutile, so that the split in the degeneracy of the two modes is smaller.

Table 1. Computed CO_2 Vibrational Frequencies for Activated CO_2 at Reduced Bi_2O_3 – TiO_2 ^a

reduced Bi_2O_3 – TiO_2 heterostructure	CO_2 vibrational frequencies/ cm^{-1}
Rutile (110)	
Bi_4O_6 -rutile (110)	1594, 1254, 941, 774
Bi_6O_9 -rutile (110)	gas-phase CO
Anatase (101)	
Bi_4O_6 -anatase (101)	1587, 1203, 700, 531

^aOur computed vibrational frequencies of free CO_2 are 2354, 1325, and 632 cm^{-1} , which can be compared with the experimental data: 2349 cm^{-1} (C=O asymmetric stretch), 1388 cm^{-1} (C=O symmetric stretch), and 667 cm^{-1} (C=O bonding, degenerate).

In addition to the excess electrons introduced by reduction and the presence of Bi–O electronic states at the top of the valence band, the atomic structure of the supported Bi_2O_3 nanoclusters can facilitate CO_2 adsorption because of the presence of low coordinated atomic sites and the flexibility in these supported nanoclusters that allows strong relaxations after the adsorption of molecules. We can also relate these findings to the work of Walker et al.⁴⁴ on the Bi-containing pyrochlore. In this system, the surface is terminated by a Bi–O layer, similar to our Bi_2O_3 nanocluster-modified TiO_2 , and the Bi 6s/6p electronic states are mixed with O 2p states at the top of the valence band. Thus, the pyrochlore has a suitable electronic structure to permit interaction with CO_2 and an atomic structure that also facilitates the interaction with CO_2 .

Given that the adsorption of CO_2 is the crucial first step in the catalytic conversion of CO_2 , which is generally not favorable or could form highly stable carbonates on metal oxides, our finding that CO_2 interacts moderately strongly with the reducible Bi_2O_3 -modified TiO_2 and can form CO or a carboxyl intermediate is a key result of this work.

3.3. CO_2 Adsorption at Oxidized Bi_2O_3 – TiO_2 Heterostructures. Table 2 presents the computed adsorption

Table 2. Computed Adsorption Energies, in eV, of CO_2 at Bi_2O_3 -Modified Rutile (110) and Anatase (101) Heterostructures

adsorption configuration	E_{ads}/eV
On Rutile (110)	
Bi_4O_6 -rutile (110) + CO_2	−0.37
Bi_6O_9 -rutile (110) + CO_2	−0.54
Bi_6O_9 -rutile (110) + CO_2 (linear)	−0.28
Bi_6O_9 -rutile (110) + CO_2	−1.01
On Anatase (101)	
Bi_4O_6 -anatase (101) + CO_2 (linear)	−0.51
Bi_4O_6 -anatase (101) + CO_2	−0.82

energies of the two most stable adsorption configurations of CO_2 at each oxidized Bi_2O_3 – TiO_2 heterostructure, and Figure 6 shows the relaxed atomic structures for these CO_2 adsorption configurations. From Table 2, we can see that there is at least one moderately strong interacting CO_2 adsorption configuration at each Bi_2O_3 – TiO_2 heterostructure, with the computed adsorption energies of −0.54, −1.01, and −0.82 eV on Bi_4O_6 -rutile, Bi_6O_9 -rutile, and Bi_4O_6 -anatase, respectively. Compared to the computed adsorption energies of CO_2 on other oxidized metal oxide-modified TiO_2 systems, for example, in ref 47 or on polymorphs of TiO_2 itself,^{10,30,31} the adsorption energies of CO_2 on Bi_2O_3 -modified TiO_2 are

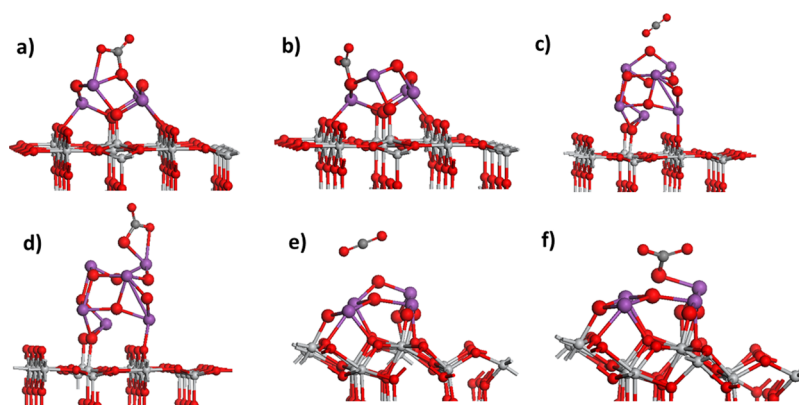


Figure 6. Relaxed adsorption structures of CO₂ at Bi₂O₃-modified rutile (110) and anatase (101) composites; the composition is indicated in each case. (a,b) CO₂ adsorption at Bi₄O₆-rutile (110) (c,d) CO₂ adsorption at Bi₆O₉-rutile (110), and (e,f) CO₂ adsorption at Bi₄O₆-anatase (101). The color coding is the same as in Figure 3.

notably stronger, indicating that these heterostructures are more favorable toward CO₂ adsorption, although we note that there is no direct formation of CO or carboxylate, suggesting that the oxidized Bi₂O₃-TiO₂ heterostructures may facilitate CO₂ capture.

Examining the atomic structures for the adsorbed CO₂, we see that there are adsorption configurations on Bi₆O₉-rutile and Bi₄O₆-anatase, namely the configurations in Figure 6c,e, which have the weakest interactions and show a linear CO₂ that is unchanged from the gas phase. This is a CO₂ physisorption mode, which we do not expect to be important.

The other adsorption modes in Figure 6 are of more interest, and these show new C–O interactions with the supported nanoclusters, and the adsorption structure is consistent with a carbonate-like adsorption mode, albeit without the strong stabilization usually found for carbonate adsorption,^{64,65} and consistent with the CO₂ adsorption on the Bi-oxide-terminated pyrochlore.⁴⁴

Table 3 presents the important C–O distances, O–C–O bending angles, and the computed CO₂ vibrational modes. The common feature of these adsorption modes of CO₂ is that the molecule is clearly bent (gas-phase CO₂ is linear, with an O–C–O angle of 180°). The O–C–O angles in the adsorbed CO₂ are 131°, 127°, and 130° on Bi₄O₆-rutile, Bi₆O₉-rutile,

and Bi₄O₆-anatase. This is consistent with the bending of activated CO₂ observed on other materials, including transition-metal carbides, or on ceria-modified rutile (110).^{4,77,78}

On Bi₄O₆-rutile, the C–O distances in the adsorbed CO₂ elongate to 1.26 and 1.27 Å, whereas the C–O distance to nanocluster oxygen is 1.39 Å. This is a notable elongation in the C–O distances over those in the gas-phase molecule (which is 1.16 Å). Similarly, on Bi₆O₉-rutile, the resulting bidentate adsorption configuration has elongated C–O distances of 1.26 and 1.29 Å in the molecule, whereas the C–O distance to the nanocluster is 1.39 Å. On Bi₄O₆-anatase, the carbon atom binds in a monodentate fashion to one oxygen in the nanocluster, with a C–O distance of 1.39 Å, whereas the C–O distances in the molecule are 1.26 and 1.27 Å.

Clearly, on Bi₂O₃-modified TiO₂, although the CO₂ molecule does not adsorb in a typical carbonate adsorption mode in which the three C–O distances are equal (~1.29 Å) and the O–C–O angles are 120°, we can nonetheless describe the adsorption as carbonate-like. Although a new C–O interaction with a C–O distance of 1.39 Å is present, we can propose that this interaction participates in helping to stabilize the adsorbed CO₂, so that it can further interact with hydrogen (see Section 3.3).

We have also computed the vibrational modes of adsorbed CO₂ on Bi₂O₃-modified TiO₂. Upon the adsorption of CO₂ at the oxidized Bi₂O₃-TiO₂ heterostructures, there are significant red shifts in the asymmetric C=O stretch of 737, 823, and 761 cm^{−1} on Bi₄O₆-rutile, Bi₆O₉-rutile, and Bi₄O₆-anatase, respectively. The degeneracy of the O–C–O bending mode is lifted upon adsorption at Bi₂O₃-TiO₂. CO₂ adsorbed on Bi₆O₉-rutile shows the largest red shift of the C=O stretch, which is consistent with its larger adsorption energy and distortions away from the gas-phase CO₂ geometry. This shift in the C=O stretching mode correlates with the strength of the CO₂-Bi₂O₃-TiO₂ interaction, and it has been observed in the experimental studies of CO₂ adsorption on a range of materials.^{79–81}

Finally, we briefly examine the electronic structure. Figure 7 shows the PEDOS for C and O atoms in CO₂, and Ti and Bi atoms, as the examples of CO₂ adsorbed on Bi₆O₉-rutile and Bi₄O₆-anatase. In both cases, the CO₂-derived C 2p and O 2p electronic states lie at the top of the valence band. Furthermore, there is a strong interaction between the Bi 6s/

Table 3. Computed C–O and Bi–O Distances and CO₂ Vibrational Frequencies for CO₂ Adsorbed at Bi₂O₃-Modified Rutile (110) and Anatase (101)^a

structure	C–O/Å	O–C–O angle/°	CO ₂ vibrational frequencies/cm ^{−1}
Rutile (110)			
Bi ₄ O ₆ -rutile (110) + CO ₂	1.27, 1.26, 1.39	131	1617, 1250, 924, 774
Bi ₆ O ₉ -rutile (110) + CO ₂	1.26, 1.29, 1.39	127	1531, 1304, 1028, 774
Anatase (101)			
Bi ₄ O ₆ -anatase (101) + CO ₂	1.26, 1.27, 1.39	130	1593, 1243, 917, 790

^aThe first two C–O distances in column 2 are in the adsorbed molecule and the third C–O distance is to oxygen in the Bi₂O₃ nanocluster. Our computed vibrational frequencies of free CO₂ are 2354, 1325, and 632 cm^{−1}, with the latter being degenerate.

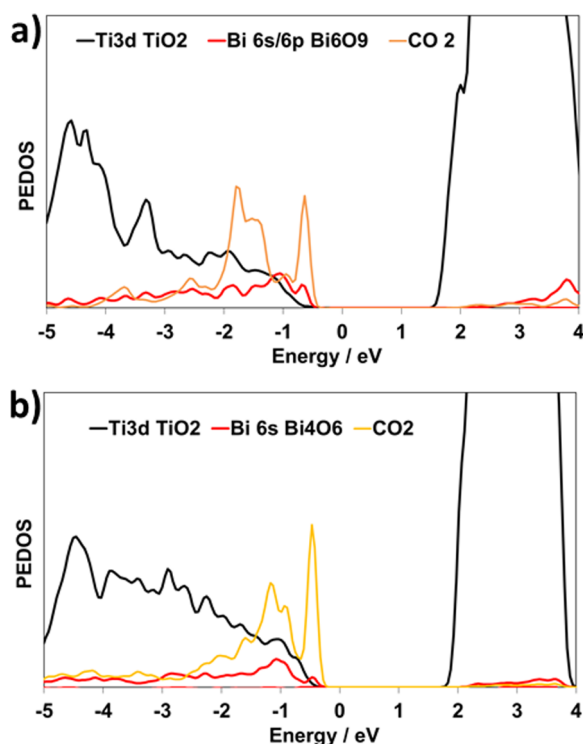


Figure 7. PEDOS projected onto the Ti 3d, Bi 6s/6p, and CO₂ 2p states after the adsorption of CO₂ onto (a) Bi₆O₉-rutile and (b) Bi₄O₆-anatase.

6p states and the carbon and oxygen 2p states of CO₂. This is consistent with the strong interaction and distortion of CO₂ when adsorbed at the supported Bi₂O₃ nanoclusters. We have also computed the Bader atomic charges upon CO₂ adsorption. These do not show a significant charge transfer between Bi₂O₃–TiO₂ and CO₂, indicating that there is no charge transfer upon the adsorption of CO₂.

In understanding the strong CO₂ adsorption without any significant charge transfer, we consider the atomic and electronic structures of Bi₂O₃ nanocluster-modified TiO₂. The nature of the valence band of Bi₂O₃–TiO₂, with high-lying Bi₂O₃-derived electronic states, permits the interaction of these Bi–O electronic states with the C and O atoms of CO₂. This can be considered similar to the case of the alkaline earth oxides, which show increased basicity and higher energy valence band states on going from Mg to Ca to Ba, and the interaction with CO₂ is stronger with the increased basic character along this series.

3.4. Hydrogenation of Adsorbed CO₂. Starting from the CO₂ adsorption structures in Section 3.3, which show moderate adsorption energies and distortions to CO₂ but no direct CO formation, we first examined the dissociation and formation of CO and adsorbed oxygen. However, such starting structures relax back to those already described, and if we remove CO, this is endothermic by up to 3 eV.

We have therefore examined the first steps in hydrogenation to explore if the adsorbed CO₂ species can be hydrogenated. We focus on Bi₄O₆-rutile and Bi₄O₆-anatase, with the most favorable CO₂ adsorption modes discussed above. We adsorb a hydrogen atom at the Bi₂O₃–TiO₂ heterostructure to simulate the dissociation of H₂ and the formation of a hydroxyl on the nanocluster. We then use the climbing image NEB method with three images to determine the activation barrier for H

migration, from which either a formate or carboxyl species can be produced.

Figure 8a,b shows the structure of the H atom adsorbed as a hydroxyl on Bi₄O₆-rutile and Bi₄O₆-anatase. The energy gain

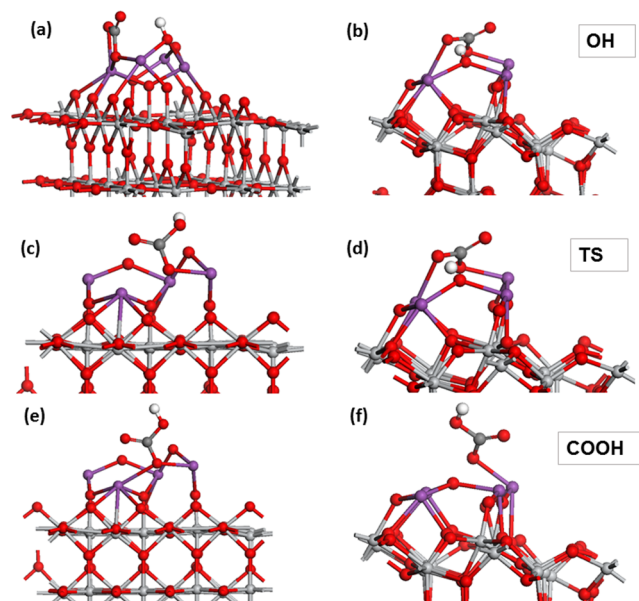


Figure 8. (a) Atomic structure of a hydroxyl species on Bi₄O₆-rutile with adsorbed CO₂. Hydrogen is denoted by the white sphere. (b) Atomic structure of a hydroxyl species on Bi₄O₆-anatase with adsorbed CO₂. (c) Atomic structure of the transition state for H migration to adsorbed CO₂ on Bi₄O₆-rutile. (d) Atomic structure of the transition state for H migration to adsorbed CO₂ on Bi₄O₆-anatase. (e) Atomic structure of a COOH intermediate on Bi₄O₆-rutile. (f) Atomic structure of a COOH intermediate on Bi₄O₆-anatase.

relative to 1/2 H₂ (in gas phase) is 1.42 eV on Bi₄O₆-rutile and 0.63 eV on Bi₄O₆-anatase. These are moderate energy gains for hydrogen adsorption. Upon H adsorption at Bi₄O₆-rutile, the O–H distance is 0.98 Å, and the Bi–O distances involving this oxygen are 2.25 and 2.44 Å. On Bi₄O₆-anatase, the O–H distance is 1.01 Å, and the Bi–O distances for this oxygen are 2.31 and 2.18 Å.

The computed barrier for H migration from the hydroxyl to oxygen in CO₂ to form a carboxyl intermediate is 0.77 eV on Bi₄O₆-rutile (110) and 0.68 eV on Bi₄O₆-anatase (101). These are moderate barriers for the H transfer to the adsorbed CO₂. The atomic structure of the transition state is shown in Figure 8c,d. In the transition state on Bi₄O₆-rutile, the H atom has migrated away from the nanocluster toward the oxygen of the adsorbed CO₂. On Bi₄O₆-anatase, the transition state involves the H atom migrating away from the oxygen of the nanocluster by 0.25 Å toward CO₂.

The atomic structure of the carboxyl intermediate on Bi₄O₆-rutile and Bi₄O₆-anatase is shown in Figure 8e,f. For the COOH intermediates, the C=O, C–O(H), OH, and C–O(Bi) distances are presented in Table 4. We also examined the formation of a formate intermediate. However, formate either lies higher by ca. 3 eV, on Bi₄O₆-rutile, or is not stable, relaxing to COOH on Bi₄O₆-anatase, and thus the COOH intermediate is preferred. If we introduce a second hydrogen atom to make COOH₂, this always relaxes to water and CO₂, removing oxygen from the Bi₂O₃ nanocluster, and thus we

Table 4. Computed C=O, C–O(H), OH, and C–O(Bi) Distances in COOH Intermediates on Bi₄O₆-Rutile and Bi₄O₆-Anatase in Å

Bi ₄ O ₆ -rutile (110)		Bi ₄ O ₆ -anatase (101)	
C=O	1.24	C=O	1.24
C–O(H)	1.35	C–O(H)	1.37
OH	0.98	OH	0.98
C–O(Bi)	1.31	C–O(Bi)	1.31

conclude that although CO₂ can adsorb at the oxidized Bi₂O₃–TiO₂ nanoclusters, it is difficult to hydrogenate to useful products.

4. CONCLUSIONS

We have studied the interaction and activation of CO₂ at the novel heterostructure of Bi₂O₃ nanoclusters supported on rutile and anatase TiO₂ surfaces. Previous experimental work has demonstrated that Bi-containing materials can activate and convert CO₂ to more useful molecules, but the origin of this is not yet clear.

The Bi₂O₃–TiO₂ heterostructures can be reduced, with moderate energy costs, which should be possible through a thermochemical process or by the addition of hydrogen. This results in the reduction of Ti sites, and Bi sites in the nanocluster can also be reduced. The interaction of the reduced heterostructures with CO₂ can result in direct exothermic CO formation, or charge transfer to CO₂ (reoxidizing Bi and Ti cations), to give an activated carboxylate species. The CO can be removed, and the addition of hydrogen is an exothermic process that forms water and reduces the nanocluster. This suggests a promising approach for CO₂ conversion via CO.

We find that CO₂ adsorbs moderately strongly at the oxidized Bi₂O₃–TiO₂ heterostructures, with the computed adsorption energies ranging from –0.54 to 1.01 eV; van der Waals interactions simply shift these energies by ca. 0.15 eV, but do not change the overall trends. CO₂ adsorbs in a carbonate-like adsorption mode (but is not overstabilized), with no charge transfer to the molecule. Finally, the computed vibrational modes of the adsorbed CO₂ show a significant red shift of over 750 cm^{–1} in the C=O stretching mode and a breaking of the degeneracy in the O–C–O bending mode. The magnitude of the red shift in the C=O stretching mode correlates with the strength of the adsorption of CO₂. The position of the high-lying valence band states derived from Bi³⁺–O interactions appear to drive the activation of CO₂.

We find that the CO₂ adsorbed in this fashion can be hydrogenated to a COOH intermediate, with the migration barriers from the nanocluster to the adsorbed CO₂ of less than 0.8 eV, whereas CO₂ dissociation is not favorable. However, further hydrogenation of COOH does not result in any useful products, and we conclude that reduction is the key to the activation and subsequent conversion of CO₂ on Bi₂O₃-modified TiO₂ heterostructures.

These results show that the unique properties of bismuth-containing oxides can be exploited to adsorb and activate carbon dioxide, which is the key first step in the reductive conversion of CO₂ to useful molecules. The combination of a non-bulk-like nanocluster-containing Bi³⁺ species, which is reducible, provides an interesting material that can activate CO₂, whether that be by strong adsorption and distortion, electron transfer to form a carboxylate, or by direct breaking of

a C–O bond, and we propose that these heterostructures can be synthesized and tested for CO₂ activation.

AUTHOR INFORMATION

Corresponding Author

*E-mail: michael.nolan@tyndall.ie.

ORCID

Michael Nolan: 0000-0002-5224-8580

Notes

The author declares no competing financial interest.

ACKNOWLEDGMENTS

Financial Support from Science Foundation Ireland through the Starting Investigator Research Grant Project EMOIN SFI/09/SRIG/I2160 and the Science Foundation Ireland US-Ireland R&D Partnership Program Project SusChem SFI/US/14/E2915 is gratefully acknowledged. Access to the computational resources at the Science Foundation Ireland/Higher Education Authority funded Irish Center for High End Computing is acknowledged. We are grateful for support from the COST Action CM1104 “Reducible Metal Oxides, Structure and Function”. We acknowledge important discussions with Profs. K. A. Gray, E. Weitz, and J. A. Byrne.

REFERENCES

- (1) Chang, X.; Wang, T.; Gong, J. CO₂ photo-reduction: insights into CO₂ activation and reaction on surfaces of photocatalysts. *Energy Environ. Sci.* **2016**, *9*, 2177–2196.
- (2) Mishra, A. K.; Roldan, A.; de Leeuw, N. H. CuO Surfaces and CO₂ Activation: A Dispersion-Corrected DFT+U Study. *J. Phys. Chem. C* **2016**, *120*, 2198–2214.
- (3) Kwon, S.; Liao, P.; Stair, P. C.; Snurr, R. Q. Alkaline-earth metal-oxide overlayers on TiO₂: application toward CO₂ photoreduction. *Catal. Sci. Technol.* **2016**, *6*, 7885–7895.
- (4) Kunkel, C.; Viñes, F.; Illas, F. Transition metal carbides as novel materials for CO₂ capture, storage, and activation. *Energy Environ. Sci.* **2016**, *9*, 141–144.
- (5) Peng, C.; Reid, G.; Wang, H.; Hu, P. Perspective: Photocatalytic reduction of CO₂ to solar fuels over semiconductors. *J. Chem. Phys.* **2017**, *147*, 030901.
- (6) Zhao, H.; Pan, F.; Li, Y. A review on the effects of TiO₂ surface point defects on CO₂ photoreduction with H₂O. *J. Materiomics* **2017**, *3*, 17–32.
- (7) Song, C. Global challenges and strategies for control, conversion and utilization of CO₂ for sustainable development involving energy, catalysis, adsorption and chemical processing. *Adsorption and Chemical Processing. Catal. Today* **2006**, *115*, 2–32.
- (8) Roy, S. C.; Varghese, O. K.; Paulose, M.; Grimes, C. A. Toward solar fuels: photocatalytic conversion of carbon dioxide to hydrocarbons. *ACS Nano* **2010**, *4*, 1259–1278.
- (9) Mikkelsen, M.; Jørgensen, M.; Krebs, F. C. The teraton challenge. A review of fixation and transformation of carbon dioxide. *Energy Environ. Sci.* **2010**, *3*, 43–81.
- (10) Habisreutinger, S. N.; Schmidt-Mende, L.; Stolarczyk, J. K. Photocatalytic Reduction of CO₂ on TiO₂ and Other Semiconductors. *Angew. Chem., Int. Ed.* **2013**, *52*, 7372–7408.
- (11) Goeppert, A.; Czaun, M.; Jones, J.-P.; Surya Prakash, G. K.; Olah, G. A. Recycling of carbon dioxide to methanol and derived products - closing the loop. *Chem. Soc. Rev.* **2014**, *43*, 7995–8048.
- (12) Varghese, O. K.; Paulose, M.; LaTempa, T. J.; Grimes, C. A. High-Rate Solar Photocatalytic Conversion of CO₂ and Water Vapor to Hydrocarbon Fuels. *Nano Lett.* **2009**, *9*, 731–737.
- (13) Varghese, O. K.; Paulose, M.; LaTempa, T. J.; Grimes, C. A. High-Rate Solar Photocatalytic Conversion of CO₂ and Water Vapor to Hydrocarbon Fuels. *Nano Lett.* **2010**, *10*, 750.

- (14) Durand, W. J.; Peterson, A. A.; Studt, F.; Abild-Pedersen, F.; Nørskov, J. K. Structure effects on the energetics of the electrochemical reduction of CO₂ by copper surfaces. *Surf. Sci.* **2011**, *605*, 1354–1359.
- (15) Mishra, A. K.; Roldan, A.; de Leeuw, N. H. A density functional theory study of the adsorption behaviour of CO₂ on Cu₂O surfaces. *J. Chem. Phys.* **2016**, *145*, 044709.
- (16) Uzunova, E. L.; Seriani, N.; Mikosch, H. CO₂ conversion to methanol on Cu(i) oxide nanolayers and clusters: an electronic structure insight into the reaction mechanism. *Phys. Chem. Chem. Phys.* **2015**, *17*, 11088–11094.
- (17) Graciani, J.; Mudiyanse, K.; Xu, F.; Baber, A. E.; Evans, J.; Senanayake, S. D.; Stacchiola, D. J.; Liu, P.; Hrbek, J.; Sanz, J. F.; Rodriguez, J. A. Highly active copper-ceria and copper-ceria-titania catalysts for methanol synthesis from CO₂. *Science* **2014**, *345*, 546–550.
- (18) Wu, H.; Zhang, N.; Wang, H.; Hong, S. Adsorption of CO₂ on Cu₂O (111) oxygen-vacancy surface: First-principles study. *Chem. Phys. Lett.* **2013**, *568–569*, 84–89.
- (19) Bendavid, L. I.; Carter, E. A. CO₂ Adsorption on Cu₂O(111): A DFT+U and DFT-D Study. *J. Phys. Chem. C* **2013**, *117*, 26048–26059.
- (20) Liu, L.; Zhao, C.; Li, Y. Spontaneous Dissociation of CO₂ to CO on Defective Surface of Cu(1)/TiO₂-x Nanoparticles at Room Temperature. *J. Phys. Chem. C* **2012**, *116*, 7904–7912.
- (21) Wu, H.; Zhang, N.; Cao, Z.; Wang, H.; Hong, S. The adsorption of CO₂, H₂CO₃, HCO₃[–] and CO₃^{2–} on Cu₂O (111) surface: First-principles study. *Int. J. Quantum Chem.* **2012**, *112*, 2532–2540.
- (22) Grabow, L. C.; Mavrikakis, M. Mechanism of Methanol Synthesis on Cu through CO₂ and CO Hydrogenation. *ACS Catal.* **2011**, *1*, 365–384.
- (23) Wang, L.; Gupta, K.; Goodall, J. B. M.; Darr, J. A.; Holt, K. B. In situ spectroscopic monitoring of CO₂ reduction at copper oxide electrode. *Faraday Discuss.* **2017**, *197*, 517–532.
- (24) Favaro, M.; Xiao, H.; Cheng, T.; Goddard, W. A.; Yano, J.; Crumlin, E. J. Subsurface oxide plays a critical role in CO₂ activation by Cu(111) surfaces to form chemisorbed CO₂, the first step in reduction of CO₂. *Proc. Natl. Acad. Sci. U.S.A.* **2017**, *114*, 6706–6711.
- (25) Peterson, A. A.; Abild-Pedersen, F.; Studt, F.; Rossmeisl, J.; Nørskov, J. K. How copper catalyzes the electroreduction of carbon dioxide into hydrocarbon fuels. *Energy Environ. Sci.* **2010**, *3*, 1311–1315.
- (26) Wu, H.; Zhang, N.; Wang, H.; Hong, S. Adsorption of CO₂ on Cu₂O (111) oxygen-vacancy surface: First-principles study. *Chem. Phys. Lett.* **2013**, *568–569*, 84–89.
- (27) Gao, D.; Zegkinoglou, I.; Divins, N. J.; Scholten, F.; Sinev, I.; Grosse, P.; Roldan Cuenya, B. Plasma-activated copper nanocube catalysts for efficient carbon dioxide electroreduction to hydrocarbons and alcohols. *ACS Nano* **2017**, *11*, 4825–4831.
- (28) Mistry, H.; Varela, A. S.; Bonifacio, C. S.; Zegkinoglou, I.; Sinev, I.; Choi, Y.-W.; Kisslinger, K.; Stach, E. A.; Yang, J. C.; Strasser, P.; Cuenya, B. R. Highly selective plasma-activated copper catalysts for carbon dioxide reduction to ethylene. *Nat. Commun.* **2016**, *7*, 12123.
- (29) Akhade, S. A.; Luo, W.; Nie, X.; Asthagiri, A.; Janik, M. J. Theoretical insight on reactivity trends in CO₂ electroreduction across transition metals. *Catal. Sci. Technol.* **2016**, *6*, 1042–1053.
- (30) Indrakanti, V. P.; Kubicki, J. D.; Schobert, H. H. Photoinduced activation of CO₂ on TiO₂ surfaces; Quantum chemical modeling of CO₂ adsorption on oxygen vacancies. *Fuel Process. Technol.* **2011**, *92*, 805–811.
- (31) Pipornpong, W.; Wanbayor, R.; Ruangpornvisuti, V. Adsorption of CO₂ on the perfect and oxygen vacancy defect surfaces of anatase TiO₂ and its photocatalytic mechanism of conversion to CO. *Appl. Surf. Sci.* **2011**, *257*, 10322–10328.
- (32) Lee, D.; Kanai, Y. Role of four-fold coordinated titanium and quantum confinement in CO₂ reduction at titania surface. *J. Am. Chem. Soc.* **2012**, *134*, 20266–20269.
- (33) Yin, W.-J.; Wen, B.; Bandaru, S.; Krack, M.; Lau, M. W.; Liu, L.-M. The effect of excess electron and hole on CO₂ adsorption and activation on rutile (110) surface. *Sci. Rep.* **2016**, *6*, 23298.
- (34) Yang, C.-T.; Wood, B. C.; Bhethanabotla, V. R.; Joseph, B. CO₂ Adsorption on Anatase TiO₂ (101) Surfaces in the Presence of Subnanometer Ag/Pt Clusters: Implications for CO₂ Photoreduction. *J. Phys. Chem. C* **2014**, *118*, 26236–26248.
- (35) Behrens, M.; Studt, F.; Kasatkin, I.; Kuhl, S.; Havecker, M.; Abild-Pedersen, F.; Zander, S.; Girgsdies, F.; Kurr, P.; Knief, B.-L.; Tovar, M.; Fischer, R. W.; Nørskov, J. K.; Schlögl, R. The Active Site of Methanol Synthesis over Cu/ZnO/Al₂O₃ Industrial Catalysts. *Science* **2012**, *336*, 893–897.
- (36) Wang, Y.; Zhao, J.; Wang, T.; Li, Y.; Li, X.; Yin, J.; Wang, C. CO₂ photoreduction with H₂O vapor on highly dispersed CeO₂/TiO₂ catalysts: Surface species and their reactivity. *J. Catal.* **2016**, *337*, 293–302.
- (37) Graciani, J.; Sanz, J. F. Designing a new generation of catalysts: Water gas shift reaction example. *Catal. Today* **2015**, *240*, 214–219.
- (38) Park, J. B.; Graciani, J.; Evans, J.; Stacchiola, D.; Senanayake, S. D.; Barrio, L.; Liu, P.; Sanz, J. F.; Hrbek, J.; Rodriguez, J. A. Gold, Copper, and Platinum Nanoparticles Dispersed on CeO_x/TiO₂(110) Surfaces: High Water-Gas Shift Activity and the Nature of the Mixed-Metal Oxide at the Nanometer Level. *J. Am. Chem. Soc.* **2009**, *132*, 356–363.
- (39) Park, J. B.; Graciani, J.; Evans, J.; Stacchiola, D.; Ma, S.; Liu, P.; Nambu, A.; Sanz, J. F.; Hrbek, J.; Rodriguez, J. A. High catalytic activity of Au/CeO_x/TiO₂(110) controlled by the nature of the mixed-metal oxide at the nanometer level. *Proc. Natl. Acad. Sci. U.S.A.* **2009**, *106*, 4975–4980.
- (40) DiMeglio, J. L.; Rosenthal, J. Selective Conversion of CO₂ to CO with High Efficiency Using an Inexpensive Bismuth-Based Electrocatalyst. *J. Am. Chem. Soc.* **2013**, *135*, 8798–8801.
- (41) Medina-Ramos, J.; DiMeglio, J. L.; Rosenthal, J. Efficient Reduction of CO₂ to CO with High Current Density Using In Situ or ex Situ Prepared Bi-Based Materials. *J. Am. Chem. Soc.* **2014**, *136*, 8361–8367.
- (42) Medina-Ramos, J.; Pupillo, R. C.; Keane, T. P.; DiMeglio, J. L.; Rosenthal, J. Efficient Conversion of CO₂ to CO Using Tin and Other Inexpensive and Easily Prepared Post-Transition Metal Catalysts. *J. Am. Chem. Soc.* **2015**, *137*, 5021–5027.
- (43) Zhang, Z.; Chi, M.; Veith, G. M.; Zhang, P.; Lutterman, D. A.; Rosenthal, J.; Overbury, S. H.; Dai, S.; Zhu, H. Rational Design of Bi Nanoparticles for Efficient Electrochemical CO₂ Reduction: The Elucidation of Size and Surface Condition Effects. *ACS Catal.* **2016**, *6*, 6255–6264.
- (44) Walker, R. J.; Pougin, A.; Oropeza, F. E.; Villar-Garcia, I. J.; Ryan, M. P.; Strunk, J.; Payne, D. J. Surface Termination and CO₂ Adsorption onto Bismuth Pyrochlore Oxides. *Chem. Mater.* **2016**, *28*, 90–96.
- (45) Walsh, A.; Payne, D. J.; Egdel, R. G.; Watson, G. W. Stereochemistry of post-transition metal oxides: revision of the classical lone pair model. *Chem. Soc. Rev.* **2011**, *40*, 4455–4463.
- (46) Walsh, A.; Watson, G. W. Polymorphism in Bismuth Stannate: A First-Principles Study. *Chem. Mater.* **2007**, *19*, 5158–5164.
- (47) Fronzi, M.; Daly, W.; Nolan, M. Reactivity of metal oxide nanocluster modified rutile and anatase TiO₂: Oxygen vacancy formation and CO₂ interaction. *Appl. Catal. A* **2016**, *521*, 240–249.
- (48) Nolan, M.; Iwaszuk, A.; Lucid, A. K.; Carey, J. J.; Fronzi, M. Design of Novel Visible Light Active Photocatalyst Materials: Surface Modified TiO₂. *Adv. Mater.* **2016**, *28*, 5425–5446.
- (49) Fronzi, M.; Iwaszuk, A.; Lucid, A.; Nolan, M. Metal oxide nanocluster-modified TiO₂ as solar activated photocatalyst materials. *J. Phys.: Condens. Matter* **2016**, *28*, 074006.
- (50) Tada, H.; Jin, Q.; Iwaszuk, A.; Nolan, M. Molecular-scale transition metal oxide nanocluster surface-modified titanium dioxide as solar-activated environmental catalysts. *J. Phys. Chem. C* **2014**, *118*, 12077–12086.
- (51) Iwaszuk, A.; Lucid, A. K.; Razeed, K. M.; Nolan, M. First principles investigation of anion-controlled red shift in light

absorption in ZnX (X = O, S, Se) nanocluster modified rutile TiO₂. *J. Mater. Chem. A* **2014**, *2*, 18796–18805.

(52) Iwaszuk, A.; Nolan, M. SnO-nanocluster modified anatase TiO₂ photocatalyst: exploiting the Sn(II) lone pair for a new photocatalyst material with visible light absorption and charge carrier separation. *J. Mater. Chem. A* **2013**, *1*, 6670–6677.

(53) Iwaszuk, A.; Nolan, M.; Jin, Q.; Fujishima, M.; Tada, H. Origin of the visible-light response of nickel(II) oxide cluster surface modified titanium(IV) dioxide. *J. Phys. Chem. C* **2013**, *117*, 2709–2718.

(54) Jin, Q.; Fujishima, M.; Iwaszuk, A.; Nolan, M.; Tada, H. Loading effect in copper(II) oxide cluster-surface-modified titanium(IV) oxide on visible- and UV-light activities. *J. Phys. Chem. C* **2013**, *117*, 23848–23857.

(55) Jin, Q.; Fujishima, M.; Nolan, M.; Iwaszuk, A.; Tada, H. Photocatalytic Activities of Tin(IV) Oxide Surface-Modified Titanium(IV) Dioxide Show a Strong Sensitivity to the TiO₂ Crystal Form. *J. Phys. Chem. C* **2012**, *116*, 12621–12626.

(56) Nolan, M. First-Principles Prediction of New Photocatalyst Materials with Visible-Light Absorption and Improved Charge Separation: Surface Modification of Rutile TiO₂ with Nanoclusters of MgO and Ga₂O₃. *ACS Appl. Mater. Interfaces* **2012**, *4*, 5863–5871.

(57) Iwaszuk, A.; Nolan, M. Reactivity of sub 1 nm supported clusters: (TiO₂)_n clusters supported on rutile TiO₂ (110). *Phys. Chem. Chem. Phys.* **2011**, *13*, 4963–4973.

(58) Nolan, M. Surface modification of TiO₂ with metal oxide nanoclusters: a route to composite photocatalytic materials. *Chem. Commun.* **2011**, *47*, 8617–8619.

(59) Nolan, M. Electronic coupling in iron oxide-modified TiO₂ leads to a reduced band gap and charge separation for visible light active photocatalysis. *Phys. Chem. Chem. Phys.* **2011**, *13*, 18194–18199.

(60) Rhatigan, S.; Nolan, M. Impact of surface hydroxylation in MgO-/SnO-nanocluster modified TiO₂ anatase (101) composites on visible light absorption, charge separation and reducibility. *Chin. Chem. Lett.* **2017**, *29*, 757–764.

(61) Lucid, A.; Iwaszuk, A.; Nolan, M. A first principles investigation of Bi₂O₃-modified TiO₂ for visible light Activated photocatalysis: The role of TiO₂ crystal form and the Bi³⁺ stereochemical lone pair. *Mater. Sci. Semicond. Process.* **2014**, *25*, 59–67.

(62) Iwaszuk, A.; Nolan, M. Lead oxide-modified TiO₂ photocatalyst: tuning light absorption and charge carrier separation by lead oxidation state. *Catal. Sci. Technol.* **2013**, *3*, 2000–2008.

(63) Schwartzenberg, K. C.; Hamilton, J. W. J.; Lucid, A. K.; Weitz, E.; Notestein, J.; Nolan, M.; Byrne, J. A.; Gray, K. A. Multifunctional photo/thermal catalysts for the reduction of carbon dioxide. *Catal. Today* **2017**, *280*, 65–73.

(64) Nolan, M. Alkaline earth metal oxide nanocluster modification of rutile TiO₂ (110) promotes water activation and CO₂ chemisorption. *J. Mater. Chem. A* **2018**, *6*, 9451–9466.

(65) Rhatigan, S.; Nolan, M. CO₂ and water activation on ceria nanocluster modified TiO₂ rutile (110). *J. Mater. Chem. A* **2018**, *6*, 9139–9152.

(66) Kresse, G.; Hafner, J. Ab initio molecular dynamics for liquid metals. *Phys. Rev. B: Condens. Matter Mater. Phys.* **1993**, *47*, 558–561.

(67) Kresse, G.; Hafner, J. Ab initio molecular-dynamics simulation of the liquid-metal-amorphous-semiconductor transition in germanium. *Phys. Rev. B: Condens. Matter Mater. Phys.* **1994**, *49*, 14251–14269.

(68) Kresse, G.; Furthmüller, J. Efficiency of Ab-initio Total Energy Calculations for Metals and Semiconductors using a Plane-wave Basis Set. *Comput. Mater. Sci.* **1996**, *6*, 15–50.

(69) Kresse, G.; Furthmüller, J. Efficient iterative schemes for ab initio total-energy calculations using a plane-wave basis set. *Phys. Rev. B: Condens. Matter Mater. Phys.* **1996**, *54*, 11169–11186.

(70) Kresse, G.; Joubert, D. From ultrasoft pseudopotentials to the projector augmented-wave method. *Phys. Rev. B: Condens. Matter Mater. Phys.* **1999**, *59*, 1758–1775.

(71) Blöchl, P. E. Projector augmented-wave method. *Phys. Rev. B: Condens. Matter Mater. Phys.* **1994**, *50*, 17953–17979.

(72) Perdew, J. P.; Chevary, J. A.; Vosko, S. H.; Jackson, K. A.; Pederson, M. R.; Singh, D. J.; Fiolhais, C. Atoms, molecules, solids, and surfaces: Applications of the generalized gradient approximation for exchange and correlation. *Phys. Rev. B: Condens. Matter Mater. Phys.* **1992**, *46*, 6671–6687.

(73) Anisimov, V. I.; Zaanen, J.; Andersen, O. K. Band theory and Mott insulators: Hubbard U instead of Stoner I. *Phys. Rev. B: Condens. Matter Mater. Phys.* **1991**, *44*, 943–954.

(74) Dudarev, S. L.; Botton, G. A.; Savrasov, S. Y.; Humphreys, C. J.; Sutton, A. P. Electron-energy-loss spectra and the structural stability of nickel oxide: an LSDA+U study. *Phys. Rev. B: Condens. Matter Mater. Phys.* **1998**, *57*, 1505–1509.

(75) Iwaszuk, A.; Mulheran, P. A.; Nolan, M. TiO₂ nanocluster modified-rutile TiO₂ photocatalyst: a first principles investigation. *J. Mater. Chem. A* **2013**, *1*, 2515–2525.

(76) Ha, M.-A.; Alexandrova, A. N. Oxygen vacancies of anatase(101): extreme sensitivity to the density functional theory method. *J. Chem. Theory Comput.* **2016**, *12*, 2889–2895.

(77) Vidal, A. B.; Feria, L.; Evans, J.; Takahashi, Y.; Liu, P.; Nakamura, K.; Illas, F.; Rodriguez, J. A. CO₂ Activation and Methanol Synthesis on Novel Au/TiC and Cu/TiC Catalysts. *J. Phys. Chem. Lett.* **2012**, *3*, 2275–2280.

(78) Posada-Pérez, S.; Viñes, F.; Ramirez, P. J.; Vidal, A. B.; Rodriguez, J. A.; Illas, F. The bending machine: CO₂ activation and hydrogenation on δ -MoC(001) and β -Mo₂C(001) surfaces. *Phys. Chem. Chem. Phys.* **2014**, *16*, 14912–14921.

(79) Schneider, W. F. Qualitative Differences in the Adsorption Chemistry of Acidic (CO₂, SO_x) and Amphiphilic (NO_x) Species on the Alkaline Earth Oxides. *J. Phys. Chem. B* **2004**, *108*, 273–282.

(80) Jensen, M. B.; Pettersson, L. G. M.; Swang, O.; Olsbye, U. CO₂ Sorption on MgO and CaO Surfaces: A Comparative Quantum Chemical Cluster Study. *J. Phys. Chem. B* **2005**, *109*, 16774–16781.

(81) Duan, Y.; Sorescu, D. C. CO₂ capture properties of alkaline earth metal oxides and hydroxides: A combined density functional theory and lattice phonon dynamics study. *J. Chem. Phys.* **2010**, *133*, 074508.